Bandwidth Extension in CMOS with Optimized On-Chip Inductors

Sunderarajan S. Mohan, Maria del Mar Hershenson, Stephen P. Boyd and Thomas H. Lee

Correspondence Address:

Sunderarajan S. Mohan

CIS-029

Stanford University

Stanford, CA 94305-4070
Phone: (650) 723-3658
FAX: (650) 725-3383
E-Mail: mohan@smirc.stanford.edu

The authors are with the Electrical Engineering Department, Stanford University, Stanford, CA 94305.

Abstract

We present a technique for enhancing the bandwidth of gigahertz broadband circuitry by using optimized on-chip spiral inductors as shunt-peaking elements. The series resistance of the on-chip inductor is incorporated as part of the load resistance to permit a large inductance to be realized with minimum area and capacitance. Simple, accurate inductance expressions are used in a lumped circuit inductor model to allow the passive and active components in the circuit to be simultaneously optimized. A quick and efficient global optimization method, based on *geometric programming* is discussed. The bandwidth extension technique is applied in the implementation of a 2.125Gbaud preamplifier that employs a common-gate input stage followed by a cascoded common-source stage. On-chip shunt-peaking is introduced at the dominant pole to improve the overall system performance, including a 40% increase in the transimpedance. This implementation achieves a 1.6kΩ transimpedance and a 0.6μA input referred current noise, while operating with a photodiode capacitance of 0.6pF. A fully differential topology ensures good substrate and supply noise immunity. The amplifier, implemented in a triple metal, single poly, 14GHz $f_{\mathrm{T}_{\mathrm{max}}}$, 0.5$\mu$m CMOS process, dissipates 225mW of which 110mW is consumed by the 50Ω output driver stage. The optimized on-chip inductors consume only 15% of the total area of 0.6mm^2.

I. Introduction

THe explosive growth in the commercial wired telecommunications market has generated tremendous interest in low-cost implementations of radio frequency broad band receivers. The performance of such a receiver's front-end is determined to a large extent by the preamplifier. Traditionally, this preamplifier has been fabricated in expensive GaAs and silicon bipolar technologies. However the quest for low cost solutions in the commercial market has spurred a desire to implement RF-ICs in standard CMOS technology. An additional advantage of these CMOS processes is that they permit the integration of the analog and digital components, the holy grail for "system-on-chip" solutions. The performance of CMOS technologies are improving constantly and consistently, thanks to the scaling achieved by the highly competitive microprocessor market. In fact, sub-micron CMOS technologies now exhibit sufficient performance for radio frequency applications in the $1 - 2$GHz range. This paper discusses how optimized on-chip inductors can be used to enhance the bandwidth of broad band amplifiers and thereby push the performance limits of CMOS implementations. An attractive feature of this technique is that the bandwidth enhancement comes with no additional power dissipation.

This bandwidth enhancement is achieved by shunt-peaking, a method first used in the 1940s to extend the bandwidth of television tubes. Section II describes the fundamentals of this approach and then focuses on how shunt-peaked amplifiers can be implemented in the integrated circuit environment. A new design methodology that permits a large inductance to be realized in a small area is discussed. Section III discusses how on-chip spiral inductors may be modeled using lumped circuit elements. A current sheet based approach is used to obtain simple, accurate expressions for the inductance so that all elements in the lumped model have analytical expressions. Thus, this lumped model can be incorporated in to a standard circuit design environment such as *SPICE*, thereby circumventing the inconvenient, iterative interface between an inductor simulator and a circuit design tool.

Section IV introduces a simple and efficient CAD tool for designing inductor circuits. This tool is based on geometric programming (GP), a special type of optimization problem for which very efficient *global* optimization methods have been developed. This technique enables the designer to optimize passive and active devices simultaneously. This feature allows a shunt-peaked amplifier with on-chip inductors to be optimized directly from specifications.

Section V and VI illustrate how shunt-peaking is used to improve the performance of a transimpedance preamplifier. A prototype preamplifier, intended for gigabit optical communication systems, is implemented in a 0.5μm CMOS process. The use of on-chip shunt peaking permits a 40% increase in the transimpedance with no additional power dissipation. The optimized on-chip inductors only consume 15% of the total chip area.

Section VII summarizes the main contributions of this paper.

II. Shunt Peaking

Although inductors are commonly associated with narrowband circuits, they are useful in broadband circuits as well. In this section, we study how an inductor can enhance the bandwidth of a broadband amplifier.

A. Shunt-peaked Amplification

[Figure 1 about here.]

We consider the simple common source amplifier illustrated in figure 1(a). For simplicity, we assume that the small signal frequency response of this amplifier is determined by a single dominant pole, which is determined solely by the output load resistance, R, and the load capacitance, C (figure 1(b)):

$$\frac{v_{\mathrm{out}}}{v_{\mathrm{in}}}(\omega) = \frac{g_{\mathrm{m}}R}{1 + j\omega RC}. \tag{1}$$

The introduction of an inductance, L, in series with the load resistance (figure 1(c)) transforms the frequency response of this amplifier. Now, the system has two poles and a zero, with the zero being determined by the L/R time constant, while the poles (which may or may not be complex) are dependent on the values of all three components:

$$\frac{v_{\mathrm{out}}}{v_{\mathrm{in}}}(\omega) = \frac{g_{\mathrm{m}}(R + j\omega L)}{1 + j\omega RC - \omega^2 LC} \tag{2}$$

The enhancement in bandwidth can be intuitively understood by noting that the positive reactance of the inductance is used to tune out part of the negative reactance of the capacitance.

The frequency response of this shunt peaked amplifier is characterized by the ratio of the L/R and RC time constants. This ratio is denoted by m so that $L = mR^2C$.

[Figure 2 about here.]

Figure 2 illustrates the frequency response of the shunt peaked amplifier for various values of m. The case with no shunt peaking ($m = 0$) is used as the reference so that its low frequency gain and its $\omega_{3\mathrm{dB}}$ (3dB bandwidth) are equal to one ($RC = 1$ and $g_{\mathrm{m}}R = 1$). The frequency response is plotted for the values of m listed in table I [1].

[Table 1 about here.]

As expected, the 3dB bandwidth increases as m increases. The maximum bandwidth is obtained when $m = 0.71$ and yields a 85% improvement in bandwidth. However, as can be clearly seen in the magnitude plot, this comes at the cost of significant gain peaking. A maximally flat response may be obtained for $m = 0.41$ with a still impressive bandwidth improvement of 72%.

Another interesting case occurs when $m = 0.32$. As seen in the phase plot, this best approximates a linear phase response up to the 3dB bandwidth, which is 60% higher than the case without shunt peaking. This case, called the 'optimum group delay case', is desirable for optimizing pulse fidelity in broadband systems that transmit digital signals and is used in the prototype preamplifier described in sections V and VI.

B. On-Chip Shunt-Peaking

The non-idealities of on-chip inductors present several challenges for implementing monolithic gigahertz circuitry. In shunt-peaking applications, the biggest issue is the the reduction in bandwidth improvement because of the additional parasitic capacitance introduced by the on-chip inductor.

[Table 2 about here.]

On-chip inductors are usually realized using bond-wires or on-chip spirals. Table II compares the attributes of these two implementations. Although bond wires exhibit much higher quality factors (Q) than spiral inductors, their use is constrained by the limited range of realizable inductances and large production fluctuations. Furthermore the bond-pad capacitance associated with the bond-wire can degrade performance. This capacitance is typically $\approx 70 - 200$fF, which is significant for gigahertz circuitry considering that the maximum realizable inductance is only $\approx$ 4nH. Thus, although bond wires have been used as shunt-peaking elements (figure 3), the net improvement in bandwidth is only $\approx 10\%$ [2]. Furthermore, differential implementations of shunt-peaked amplifiers experience a degradation in power supply rejection ratio (PSRR) because of the inductance mismatch between the two bond wires.

[Figure 3 about here.]

On the other hand, spiral inductors exhibit good matching and are therefore suitable for differential architectures. Furthermore, they permit a large range of inductances to be realized, albeit with smaller Q values. We will now discuss a new design methodology that circumvents this limitation of low Q.

[Figure 4 about here.]

Figure 4 illustrates how the inductor Q can be made irrelevant by partitioning the total load resistance, R, between the inductor's series resistance (R_{s}) and the external resistance, which now takes on the value of ($R - R_{\mathrm{s}}$). Therefore, the inductor's turn width, w, and spacing, s can be minimized to permit the desired inductance to be realized while minimizing the spiral area and capacitance. The minimum w is now only determined by current density considerations. The minimum turn spacing, s, is usually set by lithography limitations.

The desired inductance is now a function of both the transistor's and inductor's parasitics as well as the load capacitance and external resistance. Thus the optimization of on-chip shunt-peaking requires the simultaneous optimization of passive and active components. This scenario accentuates the limitations of using a field solver for modeling the inductor. Even if the field solver contains a general purpose optimization routine, it serves no purpose as the performance parameters of the inductor (such as Q) alone cannot specify the optimization goal. Therefore, several iterations would be needed (each requiring an interface between the field solver and the circuit simulator), before an acceptable design can be obtained.

Therefore, a lumped circuit model with analytical expressions for all the elements in terms of the spiral's geometrical parameters and process process parameters is essential to facilitate circuit design and optimization. The next section treats this subject in more detail.

III. Inductor Modeling

Significant work has gone into modeling spiral inductors using lumped circuit models [3], [4], [5], [6]. Figure 5 illustrates a commonly used model.

[Figure 5 about here.]

Although the parasitic resistors and capacitors in this model have simple physically intuitive expressions, the inductance value itself lacks a simple, accurate expression. The inductance has typically been calculated using the Greenhouse method [3], [7], [8]. Since this method operates by summing the self and mutual inductances of the segments of the spiral using the method of moments, the complexity of the calculation goes up as the square of the product or the number of sides and the number of turns. Thus, although the Greenhouse method offers sufficient accuracy and adequate speed, it cannot provide an inductor design directly from specifications, and is cumbersome for initial design.

A. Accurate Inductance Expressions

A simple and accurate expression for the inductance of a planar spiral can be obtained by approximating the sides of the spirals by symmetrical current sheets with equivalent current densities([9],[10] [11]).

[Figure 6 about here.]

For example, in the case of the square as illustrated in figure 6, we obtain four identical current sheets: the current sheets on opposite sides are parallel to one another, whereas the adjacent ones are orthogonal. Using symmetry and the fact that sheets with orthogonal current sheets have zero mutual inductance, the computation of the inductance is now reduced to evaluating the self inductance of one sheet and the mutual inductance between opposite current sheets. These self and mutual inductances are evaluated using the concepts of geometric mean distance (GMD), arithmetic mean distance (AMD) and arithmetic mean square distance (AMSD)([9], [12]). The resulting expression is:

$$L_{gmd} = \frac{\mu n^2 d_{\text{avg}} c_1}{2} \left[\ln(c_2/\rho) + c_3\rho + c_4\rho^2 \right], \tag{3}$$

where d_{avg} is the average diameter of the spiral (which is the mean of the outer and inner diameters: $d_{\text{avg}} = 0.5(d_{\text{out}} + d_{\text{in}})$) and ρ is a measure of how hollow or filled the spiral is ($\rho = \frac{d_{\text{out}} - d_{\text{in}}}{d_{\text{out}} + d_{\text{in}}}$). Thus a hollow spiral has ρ closer to 0, while a filled spiral has ρ closer to 1. The coefficients c_i are layout dependent and are shown in Table III.

[Table 3 about here.]

Although the accuracy of this expressions worsens as the ratio s/w becomes large, it exhibits a maximum error of 8% for $s \leq 3w$ [11]. Note that typical integrated spiral inductors are built with $s \leq w$ because smaller spacing improves the inter-winding magnetic coupling and reduces the area consumed by the spiral. A large spacing is only desired to reduce the inter-winding capacitance. In practice, this is not a concern as this capacitance is dwarfed by the under-pass capacitance [3].

The simple, analytical nature of this expression makes it ideal for circuit design and optimization. When combined with the lumped model shown in figure 5, it allows the designer to obtain design insight and explore engineering trade-offs quickly and easily. Thus, field solvers are now only needed to verify the final design.

IV. Optimization via geometric programming

This section presents an efficient method for the optimal design and synthesis of RF CMOS inductor circuits. The method is based on *geometric programming.*

A. Geometric programming

Let f be a real-valued function of n real, positive variables $x_1, x_2, \ldots, x_n$. It is called a *posynomial* function if it has the form

$$f(x_1, \ldots, x_n) = \sum_{k=1}^{t} c_k x_1^{\alpha_{1k}} x_2^{\alpha_{2k}} \cdots x_n^{\alpha_{nk}}$$

where $c_j \geq 0$ and $\alpha_{ij} \in \mathbf{R}$. When $t = 1$, f is called a *monomial* function. Thus, for example, $0.7 + 2x_1/x_3^2 + x_2^{0.3}$ is posynomial and $2.3(x_1/x_2)^{1.5}$ is a monomial. Posynomials are closed under sums, products, and nonnegative scaling.

A *geometric program* (GP)) has the form

$$\begin{array}{ll} \text{minimize} & f_0(x) \\ \text{subject to} & f_i(x) \leq 1, \quad i = 1, 2, \ldots, m, \\ & g_i(x) = 1, \quad i = 1, 2, \ldots, p, \\ & x_i > 0, \quad i = 1, 2, \ldots, n, \end{array} \tag{4}$$

where f_i are posynomial functions and g_i are monomial functions. If f is a posynomial and g is a monomial, then the constraint $f(x) \leq g(x)$ can be expressed as $f(x)/g(x) \leq 1$ (since f/g is posynomial). From closure under non-negativity, constraints of the form $f(x) \leq a$, where $a > 0$ can also be used. Similarly, if g_1 and g_2 are both monomial functions, the constraint $g_1(x) = g_2(x)$ can be expressed as $g_1(x)/g_2(x) = 1$ (since g_1/g_2 is monomial).

The key to solving GPs is a change of variables that converts the posynomial objective and constraint functions into *convex* functions of the new variables. We define new variables $y_i = \log x_i$, and take the logarithm of a posynomial f to get

$$h(y) = \log\left(f\left(e^{y_1}, \ldots, e^{y_n}\right)\right) = \log\left(\sum_{k}^{t} e^{a_k^T y + b_k}\right)$$

where $a_k^T = [\alpha_{1k} \cdots \alpha_{nk}]$ and $b_k = \log c_k$. It can be shown that h is a *convex* function of y. This transformation converts the standard geometric program (4) into the convex optimization program:

$$\begin{array}{ll} \text{minimize} & \log f_0(e^{y_1}, \ldots, e^{y_n}) \\ \text{subject to} & \log f_i(e^{y_1}, \ldots, e^{y_n}) \leq 0, \quad i = 1, \ldots, m \\ & \log g_i(e^{y_1}, \ldots, e^{y_n}) = 0, \quad i = 1, \ldots, p, \end{array} \tag{5}$$

which is called the *convex form* of the geometric program. Even though this problem is highly nonlinear, it can be solved globally and very efficiently by recently developed interior-point methods (see, e.g., [14]).

For our purposes, the most important feature of geometric programs is that they can be *globally* solved with great efficiency. GP solution algorithms also determine whether the problem is infeasible. Also, the starting point for the optimization algorithm does not have any effect on the final solution; indeed, an initial starting point or design is completely unnecessary.

B. Optimization of a Shunt-peaked Amplifier

Several circuit design problems may be posed as geometric programs [15], [16]. In particular, the design specifications of inductor circuits can be formulated in a way suitable for geometric programming [17]. The shunt-peaked amplifier design is a good example. As discussed earlier, in on-chip implementations, the series resistance of the spiral inductor is absorbed within the gain resistor, R, and the capacitance of the inductor C_{tot} is added to the load capacitance C_{load}. The goal is to minimize the capacitance added by the inductor so that a large bandwidth extension can be obtained. The shunt-peaked amplifier problem can therefore be written as the following geometric program:

$$\begin{array}{ll} \text{minimize} & C_{\text{tank}} \\ \text{subject to} & L_{\text{tank}} = mR^2 C_{\text{tank}} \\ & w > w_{\min} \\ & C_{\text{tank}} \geq C_{\text{load}} + C_{\text{tot}} \\ & \ldots \end{array} \tag{6}$$

V. Design Example

[Figure 7 about here.]

This section illustrates how optimized on-chip spiral inductors can improve the performance of a preamplifier intended for the front-end of a gigabit optical system. Figure 7 shows the block diagram of a typical optical communication receiver. The key performance parameters of such a front-end are bandwidth, sensitivity, stability and dynamic range. The system's bandwidth and sensitivity are determined largely by the preamplifier [18], [19], [20]. While a high bandwidth demands a small input resistance, good sensitivity requires the resistors in the signal path to be large in order to minimize thermal noise. Thus, the preamplifier is typically implemented using a transimpedance architecture as it provides a large bandwidth by synthesizing a small input resistance using a much larger feedback resistor.

A. Transimpedance Limit

[Figure 8 about here.]

Figure 8 illustrates the main elements of a transimpedance preamplifier. Assuming that the bandwidth of the amplifier is set by the input pole, we obtain:

$$\omega_{3\mathrm{dB}} = \frac{1}{R_{\mathrm{in}} C_{\mathrm{in}}}, \tag{7}$$

where $\omega_{3\mathrm{dB}}$ is the 3dB bandwidth of the circuit, R_{in} is the input resistance and C_{in} is total input capacitance.

R_{in} is given by:

$$R_{\mathrm{in}} = \frac{R_{\mathrm{f}}}{A+1} \approx \frac{R_{\mathrm{f}}}{A} \tag{8}$$

where R_{f} is the feedback resistance and A is the open loop gain of the amplifier. The approximate expression is valid when $A >> 1$.

C_{in} is given by :

$$C_{\mathrm{in}} = C_{\mathrm{g}} + C_{\mathrm{D}}, \tag{9}$$

where C_{g} is the input gate capacitance of the amplifier and C_{D} is the sum of the capacitances of the active area of the photo-diode as well as associated parasitic capacitances (arising from bond-pads etc.). In GaAs implementations, C_{D} can be kept small by integrating the photo-diode and the preamplifier on the same die. In such technologies, C_{D} as small as $50fF$ are common [21]. Silicon Bipolar and CMOS implementations are not so fortunate: a C_{D} of $\approx 300 - 600$FF is typical.

The gain bandwidth product determines the maximum available gain for a given bandwidth. Denoting the transition frequency as ω_{T}, we relate the gain, A, to the 3dB bandwidth $\omega_{3\mathrm{dB}}$:

$$A \approx \frac{\omega_{\mathrm{T}}}{\omega_{3\mathrm{dB}}}. \tag{10}$$

Substituting equations 8-10 in to equation 7, we obtain a maximum achievable transimpedance, $R_{\mathrm{f,max}}$:

$$R_{\mathrm{f,max}} \approx \frac{\omega_{\mathrm{T}}}{\omega_{3\mathrm{dB}}^2 (C_{\mathrm{g}} + C_{\mathrm{D}})} \tag{11}$$

Noting that the transconductance, g_{m}, of the input stage is related to C_{g} by $g_{\mathrm{m}} \approx \omega_{\mathrm{T}} C_{\mathrm{g}}$, and that for optimum sensitivity, $C_{\mathrm{g}} \approx C_{\mathrm{D}}$, we conclude that the maximum achievable transimpedance is determined by the system bandwidth specification, the total input capacitance and the process constant, ω_{T}.

B. Circumventing the Transimpedance Limit

[Figure 9 about here.]

Figure 9 illustrates a modified preamplifier architecture that circumvents the transimpedance limit. The transimpedance stage is decoupled from the photo-diode by a common-gate stage and the gain-bandwidth product of the transimpedance stage is enhanced by shunt-peaking. Now, the sensitive feedback node of the transimpedance stage is more robust as its poles are not determined by any off-chip components. Furthermore, the common-gate stage permits the transistors of the transimpedance stage to be sized smaller enabling a higher transimpedance to be achieved.

Note that the common-gate stage is not necessary to obtain the benefits of shunt-peaking. If desired, one could connect the photo-diode directly to a shunt-peaked transimpedance stage. Such an implementation is particularly attractive for applications that demand the best achievable sensitivity for a given power. However, such an implementation requires the parasitic impedance of the photo-diode to be known so that the transimpedance stage can be sized for optimal performance. The introduction of the common-gate stage offers an additional degree of flexibility for the designer and permits stable operation over a wider range of photo diode capacitances. This is valuable in cases (such as our prototype) where the capacitance of the photo diode structure is not known in advance. The drawback of the common-gate source is the degradation in the high frequency noise performance due to the source junction capacitance of the common-gate transistor, an issue that will be addressed more in section V-E.

C. Shunt-peaked transimpedance stage

[Figure 10 about here.]

Figure 10 illustrates the shunt-peaked transimpedance stage. The cascode eliminates the bandwidth degradation due to the Miller capacitance of the common-source stage's gate-drain capacitance. This degradation is particularly significant in CMOS circuits, where the gate-drain capacitance can be as high as one-third of the gate-source capacitance. The cascode also enhances the overall gain by increasing the stage's output impedance.

The dominant pole in the amplifier occurs at the drain of the cascode transistor. The bandwidth of the amplifier is improved by applying shunt-peaking at this node. The inductor, resistors and transistors are sized for optimum group delay over the signal bandwidth. The design methodology can be summarized as follows:

1. Design and optimize transimpedance stage for desired signal bandwidth without shunt peaking.
2. Use transistor current and interconnect current density specification to determine inductor's turn width, w.
3. Determine minimum turn spacing, s, from process specifications.
4. Choose number of turns, n, and outer diameter d_{out} to realize optimum L while minimizing parasitic capacitance and area.
5. Increase the transimpedance resistance, R_{f}, and the total load resistance, R.

The availability of a lumped inductor model (with analytical expressions for all elements including the inductance) and the use of geometric programming allows this entire design and optimization process to be automated so that no iteration is needed on the part of the designer. In this case, a 20nH inductor was realized with an outer diameter of only 180μm. This inductor had 11.75 turns, a width of 3.2μm, a spacing of 2.1μm and was implemented on the third (top) metal layer with thickness 2.1μm. The shunt-peaking yielded a 40% increase in the transimpedance of this stage (for a fixed signal bandwidth) with no additional power dissipation. Alternatively, the shunt peaking could have been used to increase the signal bandwidth for a fixed transimpedance.

D. Differential architecture

Compared to differential architectures, single-ended architectures consume less power, take up less die-area, and exhibit better noise performance. However at high frequencies they are susceptible to supply noise and are plagued by stability problems stemming from parasitic feedback paths. By providing good common-mode rejection, differential architectures circumvent these disadvantages, and are therefore preferred in systems where the integration of the analog and digital functions is the ultimate goal. In keeping with this premise, the architecture described here is fully differential and provides complementary outputs, which is a necessity given that high-speed digital and clocking circuitry operate in differential mode.

[Figure 11 about here.]

Figure 11 shows the schematic of the complete prototype preamplifier. The common-gate (CG) stage is followed by the common-source(CS) transimpedance stage, whose output goes to a source follower that buffers the output driver. The output driver is only needed for testing purposes and is not needed nor desired in a system where the analog and digital components of a receiver are integrated.

The chip consumes a total of 225mW, of which the 50Ω output driver consumes 110mW. For optimum sensitivity, the total power consumption of the common-gate and common-source stages is roughly proportional to the photo-diode capacitance. This preamplifier has been designed to operate with an external capacitance as large as 600fF. The need to support such a large capacitance arises because the photodiodes are external to the chip with correspondingly large bondpad capacitances. Recent research has explored flip-chip bonding techniques for reducing the capacitance loading of the front-end to less than 100fF. Such a low input capacitance would permit a higher input impedance and therefore allow smaller devices to be used throughout the preamplifier, resulting in a substantial power saving, while retaining the same bandwidth and improving sensitivity. Alternatively, the reduced capacitance would allow the design of preamplifiers with increased bandwidth supporting faster baud rates.

E. Noise Considerations

The sensitivity of the preamplifier is usually expressed as the equivalent integrated input-referred current noise density. Significant work has gone in to deriving the minimum noise conditions for conventional optical preamplifiers [18], [22]. Some studies have also investigated how inductors can increase the sensitivity of optical preamplifiers implemented in GaAs [19].

The noise performance of the common-gate(CG) input stage followed by the common-source (CG) transimpedance stage has been studied in GaAs HBT and BiCMOS processes [23]. Although, a simulation involving a single-ended CMOS version was reported, it ignored the effects of the source and drain junction capacitances and did not consider the impact of short-channel effects on small signal behavior and noise [24].

Junction capacitances in sub-micron CMOS processes are comparable to the gate capacitances and therefore significantly influence both noise behavior and bandwidth. A rigorous analysis that includes the impact of the junction capacitances and short-channel behavior yields two conditions for a noise optimum. First, the saturation mode gate capacitance of the common-source stage must equal the saturation mode drain capacitance of the common-gate stage so that $C_{\mathrm{gs,CS}} + C_{\mathrm{gd,CS}} = C_{\mathrm{gd,CG}} + C_{\mathrm{db,CG}}$. Second, the saturation mode input capacitance of the common-gate stage (which is the gate-source capacitance, $C_{\mathrm{gs,CG}}$, plus the source-substrate capacitance $C_{\mathrm{sb,CG}}$) must equal βC_{ext}, where $\beta \approx 0.8 - 1$. β is a function of both devices' ω_{T}, their coefficients of channel thermal noise (γ), and their ratios of junction capacitance to gate capacitance, all of which are bias dependent. For a typical CMOS device in saturation, $(C_{\mathrm{gs}} + C_{\mathrm{sb}})$ is around 3-4 times as big as $(C_{\mathrm{gd}} + C_{\mathrm{db}})$ and therefore the common-source stage can now be sized smaller, allowing a corresponding increase in the feedback resistance and a dramatic decrease in power consumption, while retaining the same device f_T. The buffer stage that follows the common-source stage can also be sized smaller, as can the width of all the interconnects, resulting in a smaller die area. The transconductance of the common-gate stage only needs to be large enough to ensure that the input pole is non-dominant, enabling the power consumption of the first stage to be small.

The introduction of the common-gate stage introduces three new noise sources: the thermal noise of the source resistor, the thermal noise of the drain resistor, and the thermal channel noise of the common-gate transistor. Of these terms, careful design ensures that the resistors are made large enough so as not to significantly affect the noise performance. The thermal channel noises of the the common-gate and common-source devices are reflected at the input by equivalent current noise spectral densities proportional to the square of the frequency. When integrated over frequency, these terms dominate, a behavior typical of short-channel CMOS processes, where carrier velocity saturation conditions cause thermal channel noise to increase due to excess noise stemming from hot electron effects [25]. The upside is that the continuing reduction in gate length promises higher f_T CMOS devices, thereby improving noise performance. However, carrier velocity saturation causes the small signal transconductance (and f_T) to be smaller than that predicted by long channel (square-law) approximations.

VI. Layout and Experimental Details

[Figure 12 about here.]

As shown in the die photo (figure 12), the chip area is dominated by the passive components, which is typical of RF-ICs. However, the two inductors combine for less than 15% of the total area, thanks to the optimized shunt-peaking technique described in the earlier sections. A patterned ground shield is used beneath the inductors to reduce substrate coupling [26]. Differential symmetry and cross quad layout are used to ensure maximum matching, thereby reducing common-mode noise and systematic offset. 16pF of on chip capacitance is used to provide supply decoupling. Several substrate contacts, placed around the transistors, minimize source inductance. The floor plan keeps the sensitive input bond pads as far away from the other pads as possible.

[Figure 13 about here.]

Figure 13 shows the test structure of the spiral inductor used for shunt-peaking. The S-parameters of the inductor were measured using coplanar ground-signal-ground (GSG) probes and an open calibration structure. The inductance and the one-port impedance (which is the relevant measure in our amplifier) were extracted from these measurements.

[Figure 14 about here.]

As shown in figure 14, good agreement between the prediction of the lumped circuit inductor model and measured data is obtained for the equivalent one-port impedance of the spiral inductor used for shunt-peaking. In particular, we note that the measured inductance of 20.5nH matches the 20.3nH value predicted by our simple inductance expressions to within a 1% error.

Figure 15 shows the preamplifier's simulated transimpedance versus frequency for photodiode capacitances varying from 100fF to 700fF. As can be seen, the 3dB bandwidth is around 1.2GHz and only weakly dependent on the photodiode capacitance. Maximum gain peaking is 1dB. These simulations are run with the output driving a 50Ω resistance and 1pF capacitance.

[Figure 15 about here.]

Figure 16 illustrates the preamplifier's simulated equivalent input referred current noise spectral density for a photodiode capacitance of 600fF. The coefficient of channel thermal noise (γ) is varied from 2/3, the long-channel value, to 2, to discern the degradation in sensitivity due to excess noise in short channel devices. The worst case value of 2 predicts an input referred current noise of 0.6μA, a significant degradation from the 0.4μA predicted by long-channel estimates.

[Figure 16 about here.]

[Figure 17 about here.]

Figure 17(a) and Figure 17(b) display the measured single-sided output eye diagrams for operation at 2.1 and 1.6 Gbaud respectively. An open eye is obtained for single-sided output voltages extending from 4mV to 500mV. Table IV summarizes the performance of the prototype chip.

[Table 4 about here.]

VII. Conclusions

This paper presented an area and power efficient technique for boosting the bandwidth of broadband systems using optimized on-chip inductors as shunt-peaking elements. Simple, accurate inductance expressions were used in a lumped circuit inductor model to facilitate circuit design. The analytical expressions of this inductor model permitted inductor circuit problems to be posed as *geometric programs* so that globally optimal solutions could be obtained easily, with no iteration needed on the part of the designer.

These bandwidth extension and circuit optimization techniques were applied in the implementation of a 2.125Gbaud, 1.6kΩ differential transimpedance preamplifier with an equivalent input current noise of 0.6μA. The chip has a die area of $0.6mm^2$, of which less than 15% is consumed by the two inductors. Designed in a triple metal, single poly, $0.5\mu m$ CMOS process, this chip was intended as a test vehicle to demonstrate how on-chip bandwidth extension techniques can push the limits of low-cost CMOS processes. To the best of the authors' knowledge, this chip is the first CMOS amplifier to use on-chip planar, spiral inductors for bandwidth enhancement.

VIII. Acknowledgments

The authors would like to thank Rockwell International for fabricating the chips. Particularly, they are obliged to Dr. Christopher Hull and Dr. Paramjit Singh for invaluable discussions on layout and processing. They would also like to acknowledge Dr. Allen Lu, Dr. Tad Hofmeister and Prof. Leonid Kazovksy for help with the optical measurements, and to Dr. C. Patrick Yue for helpful discussions on spiral inductors.

References

[1] T. H. Lee, *The Design of CMOS Radio-Frequency Integrated Circuits*, Cambridge University Press, 1998.

[2] T. Yoon and B. Jalali, "Front-end cmos chipset for fiber-based gigabit ethernet," in *Symposium on VLSI Circuits, , Digest of Technical Papers*, June 1998, pp. 188–191.

[3] C. P. Yue, C. Ryu, J. Lau, T. H. Lee, and S. S. Wong, "A physical model for planar spiral inductors on silicon," in *Proceedings IEEE IEDM'96*, 1996.

[4] J. Crols, P. Kinget, J. Craninckx, and M. Steyeart, "An analytical model of planar inductors on lowly doped silicon substrates for analog design up to 3GHz," in *Symposium on VLSI Circuits, Digest of Technical Papers*, 1996, pp. 28–29.

[5] J. N. Burghartz, K. A. Jenkins, and M. Soyuer, "Multilevel-spiral inductors using VLSI interconnect technology," *IEEE Electron device letters*, vol. 17, no. 9, pp. 428–430, September 1996.

[6] R. B. Merrill, T. W. Lee, H. You, R. Rasmussen, and L. A. Moberly, "Optimization of high Q integrated inductors for multi-level metal CMOS," in *Proceedings IEEE IEDM'95*, 1995, pp. 38.7.1–38.7.4.

[7] K. B. Ashby, I. A. Koullias, W. C. Finley, J. J. Bastek, and S. Moinian, "High Q inductors for wireless applications in a complementary silicon bipolar process," *IEEE Journal of Solid-State Circuits*, vol. 31, no. 1, pp. 4–9, January 1996.

[8] H. M. Greenhouse, "Design of planar rectangular microelectronic inductors," *IEEE Transactions on parts, hybrids, and packaging*, vol. PHP-10, no. 2, pp. 101–109, June 1974.

[9] E. B. Rosa, "Calculation of the self-inductances of single-layer coils," *Bull. Bureau of Standards*, vol. 2, no. 2, pp. 161–187, 1906.

[10] S. S. Mohan, M. Hershenson, S. P. Boyd, and T. H. Lee, "Simple accurate expressions for planar spiral inductances," *IEEE Journal of Solid-State Circuits*, 1999, To appear.

[11] S. S. .Mohan, "Modeling, design, and optimization of on-chip inductors and transformers," PhD Oral Examination, Electrical Engineering Department, Stanford University, June 1999, http://smirc.stanford.edu.

[12] J. C. Maxwell, *A Treatise on Electricity and Magnetism*, Dover, 3 edition, 1967.

[13] R. J. Duffin, E. L. Peterson, and C. Zener, *Geometric Programming — Theory and Applications*, Wiley, 1967.

[14] Y. Nesterov and A. Nemirovsky, *Interior-point polynomial methods in convex programming*, vol. 13 of *Studies in Applied Mathematics*, SIAM, Philadelphia, PA, 1994.

[15] S. Boyd and L. Vandenberghe, "Introduction to convex optimization with engineering applications," Course Notes, 1997, `http://www-leland.stanford.edu/class/ee364/`.

[16] M. Hershenson, S. P. Boyd, and T. H. Lee, "GPCAD: A tool for CMOS op-amp synthesis," in *Digest of Technical Papers IEEE International Conference on Computer-Aided Design*, 1998, to appear.

[17] S. P. Boyd M. Hershenson, S. S. Mohan and T. H. Lee, "Optimization of inductor circuits via geometric programming," in *Design Automation Conference, session 54.3*, June 1999, pp. 994–998.

[18] R. G. Smith and S. D. Personik, "Receiver design for optical communication systems," in *Topics in Applied Physics : Semiconductor Devices for Optical Communication*, vol. 39, pp. 89–160. Springer-Verlag, Berlin, Germany, second edition, 1982.

[19] Norman Scheinberg, Robert J. Bayruns, and Timothy M. Laverick, "Monolithic GaAs transimpedance amplifiers for fiber-optic receivers," *IEEE Journal of Solid-State Circuits*, vol. 26, no. 12, pp. 1834–1839, Dec. 1991.

[20] S. S. Mohan and T. H. Lee, "A 2.125Gbaud 1.6kω transimpedance preamplifier in 0.5μm CMOS," in *Custom Integrated Circuits Conference, Digest of Technical Papers*, May 1999.

[21] Z. Lao et al., "25Gb/s AGC amplifier, 22 GHz transimpedan ce amplifier and 27.7GHz limiting amplifier ics using AlGaAs/GaAs-hemts," in *ISSCC Digest of Technical Papers*, 1997, vol. 40, pp. ??–??

[22] A. A. Abidi, "On the choice of optimum FET size in wide-band transimpedance amplifiers," *Journal of Lightwave Technology*, vol. 6, no. 1, pp. 64–66, Jan. 1988.

[23] Tongtod Vanisri and Chris Toumazou, "Integrated high frequency low-noise current-mode optical transimpedance preamplifiers: Theory and practice," *IEEE Journal of Solid-State Circuits*, vol. 30, no. 6, pp. 677–685, June 1995.

[24] C. Toumazou and S. M. Park, "Wideband low noise CMOS transimpedance amplifiers for gigahertz operation," *Electronics Letters*, vol. 32, no. 13, pp. 1194–1196, June 1996.

[25] Derek K. Shaeffer and Thomas H. Lee, "A 1.5V, 1.5GHz CMOS low-noise amplifier," *IEEE Journal of Solid-State Circuits*, vol. 32, no. 5, pp. 745–759, May 1997.

[26] C. Patrick Yue and S. Simon Wong, "On-chip spiral inductors with patterned ground shields for Si-based RF IC's," in *1997 Symposium on VLSI Circuits Digest of Technical Papers*, 1997, pp. 85–86.

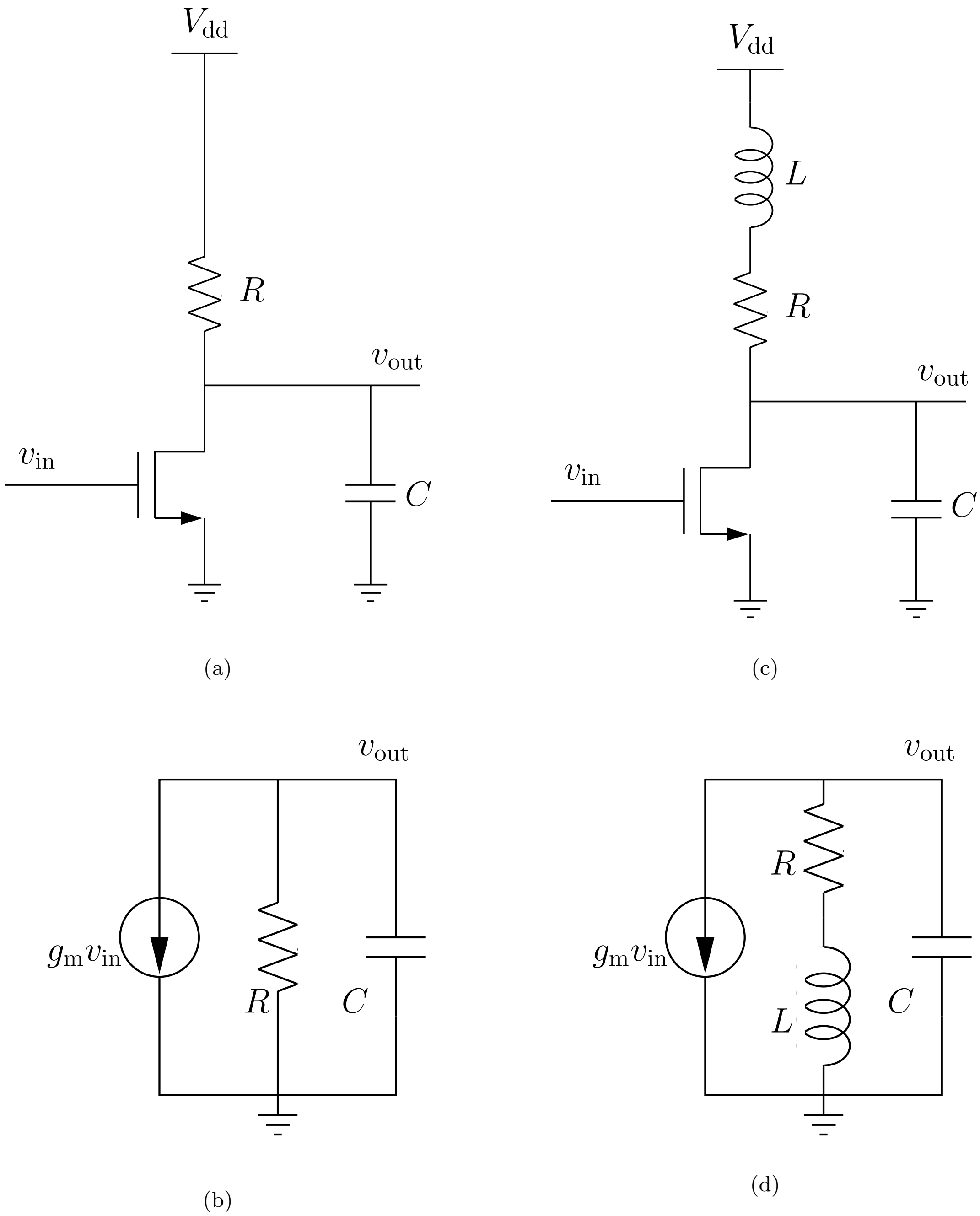

Fig. 1. Shunt-peaking a common source amplifier. (a)simple common source amplifier, and its (b) equivalent small signal model. (c)common source amplifier with shunt peaking and its (d)equivalent small signal model.

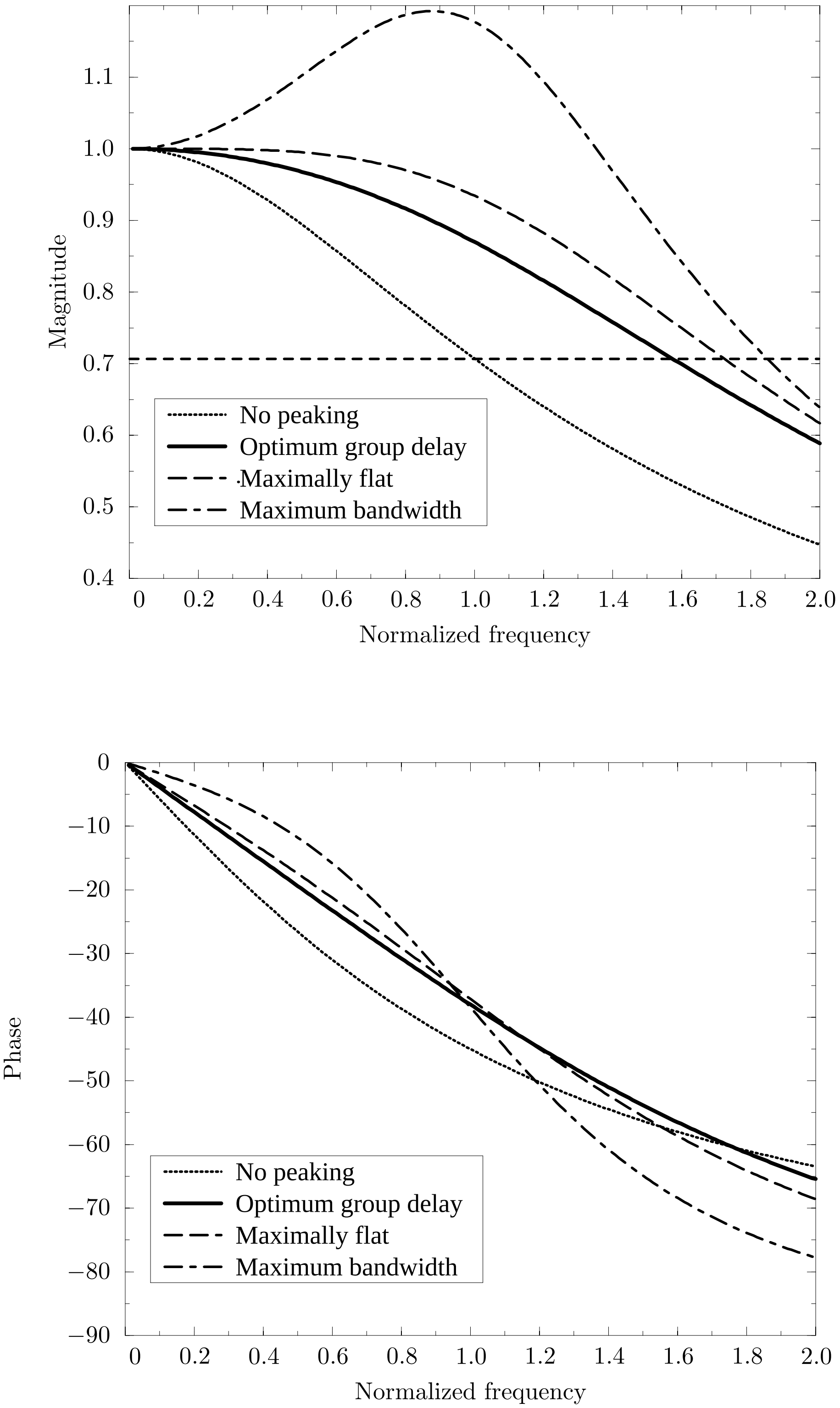

Fig. 2. Frequency response of shunt-peaked cases tabulated in table I.

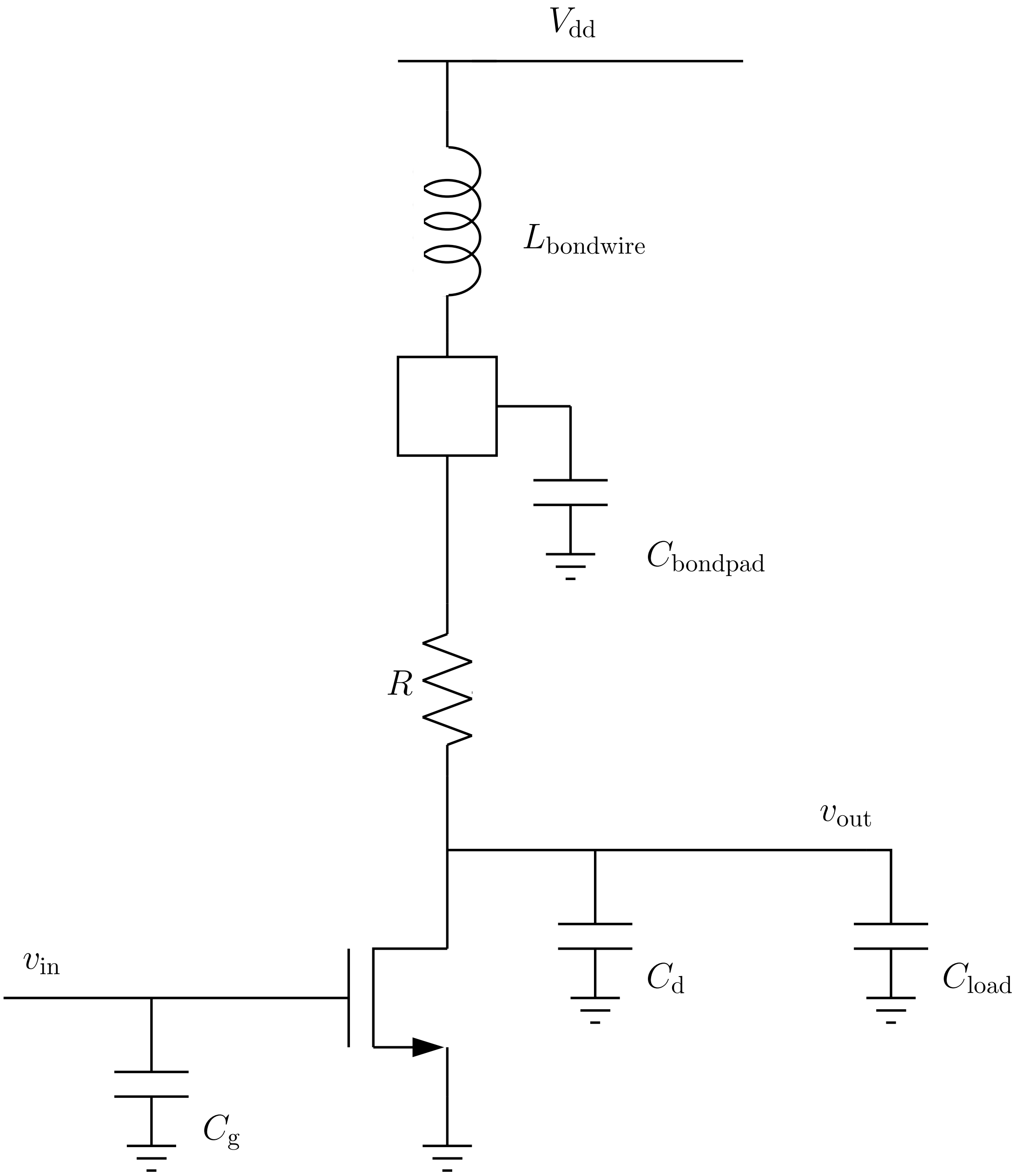

Fig. 3. Shunt-peaking with a bond wire inductor

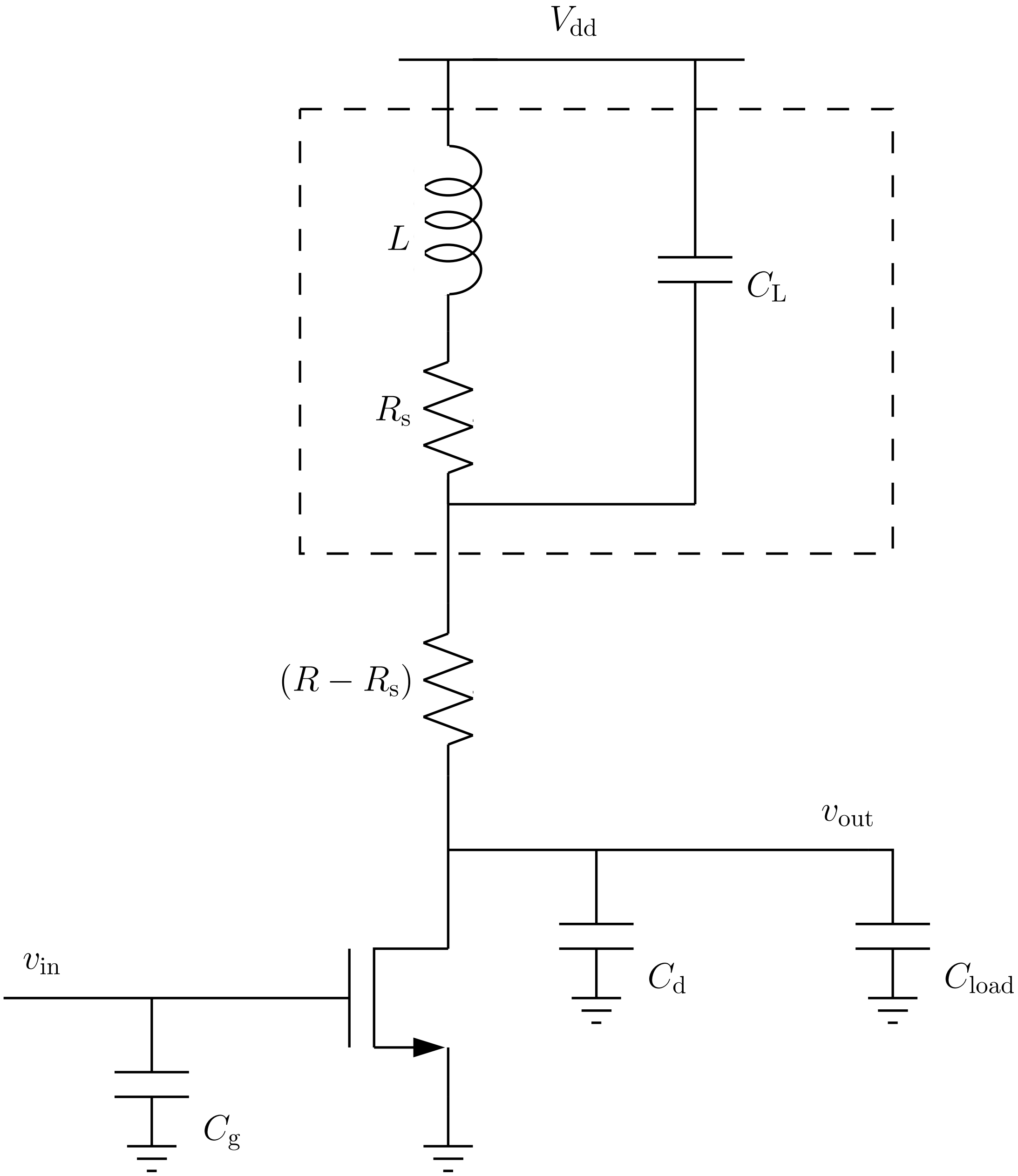

Fig. 4. Shunt-peaking with optimized on-chip inductor

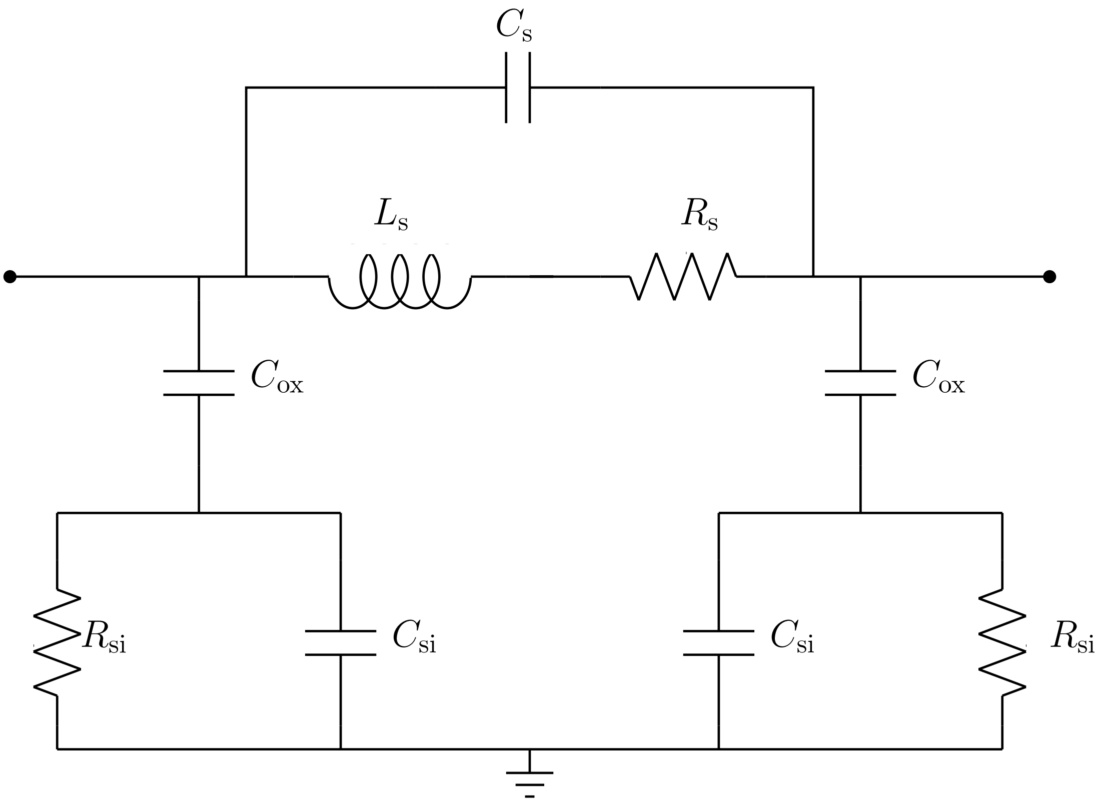

Fig. 5. Lumped inductor model.

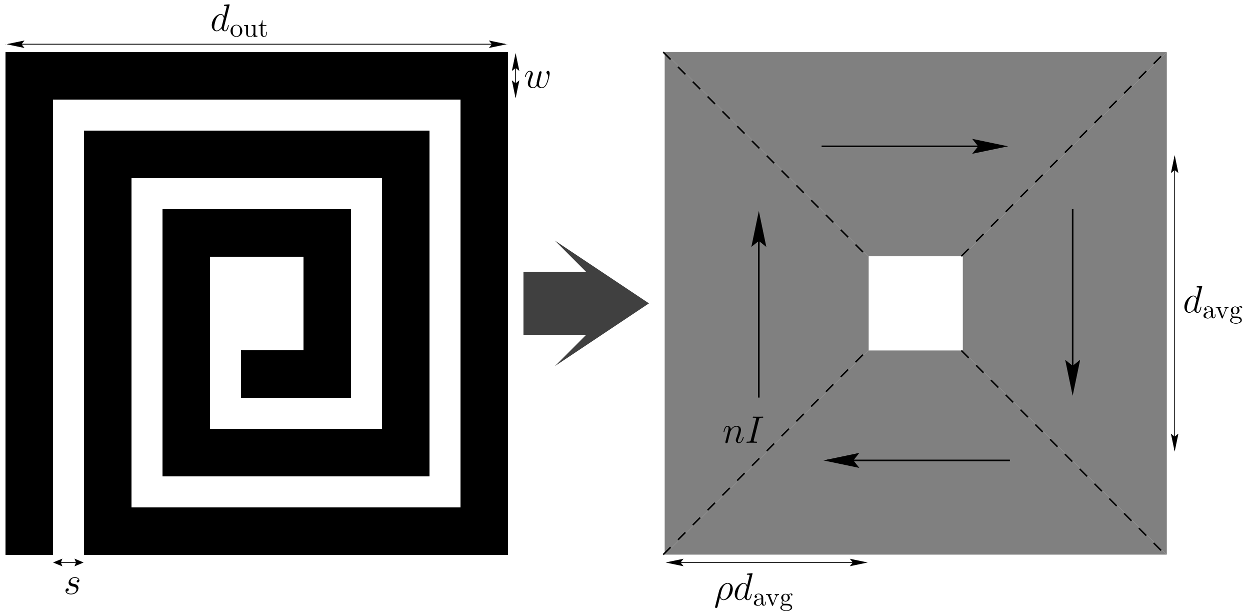

Fig. 6. Current sheet approximation of a square spiral

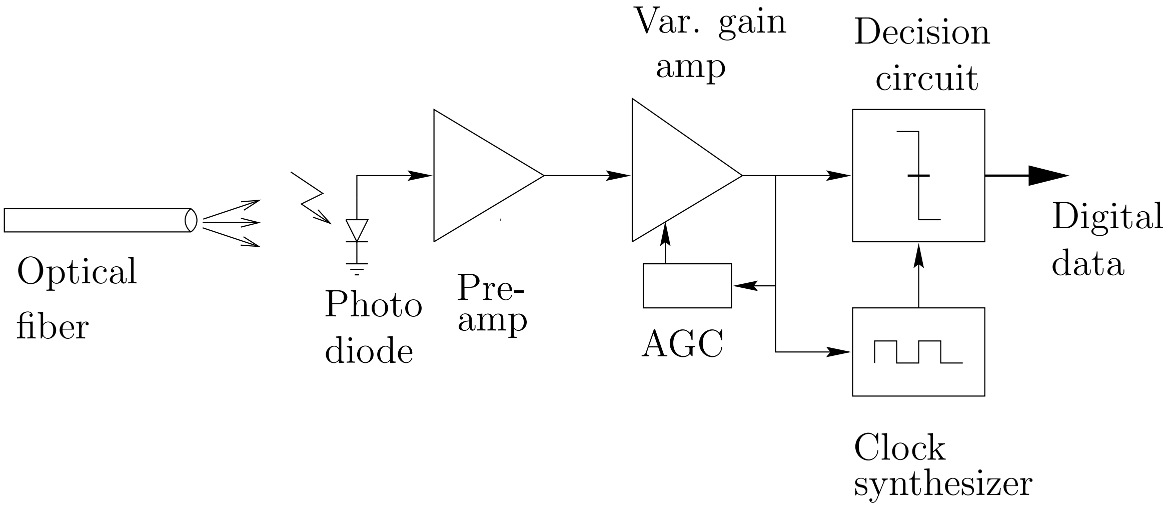

Fig. 7. System overview

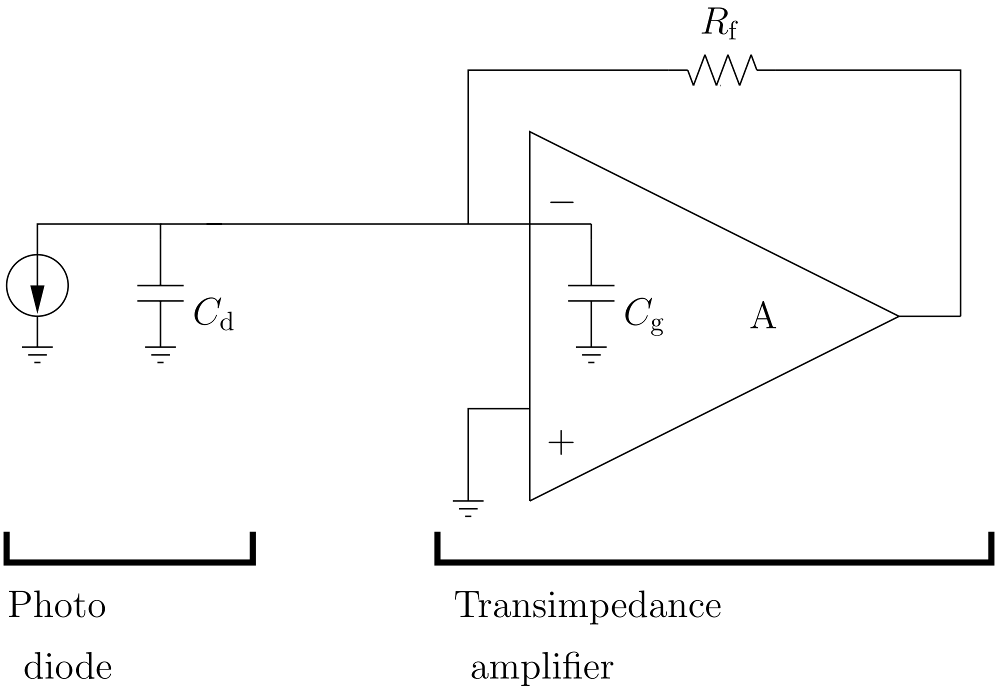

Fig. 8. Conventional preamplifier architecture

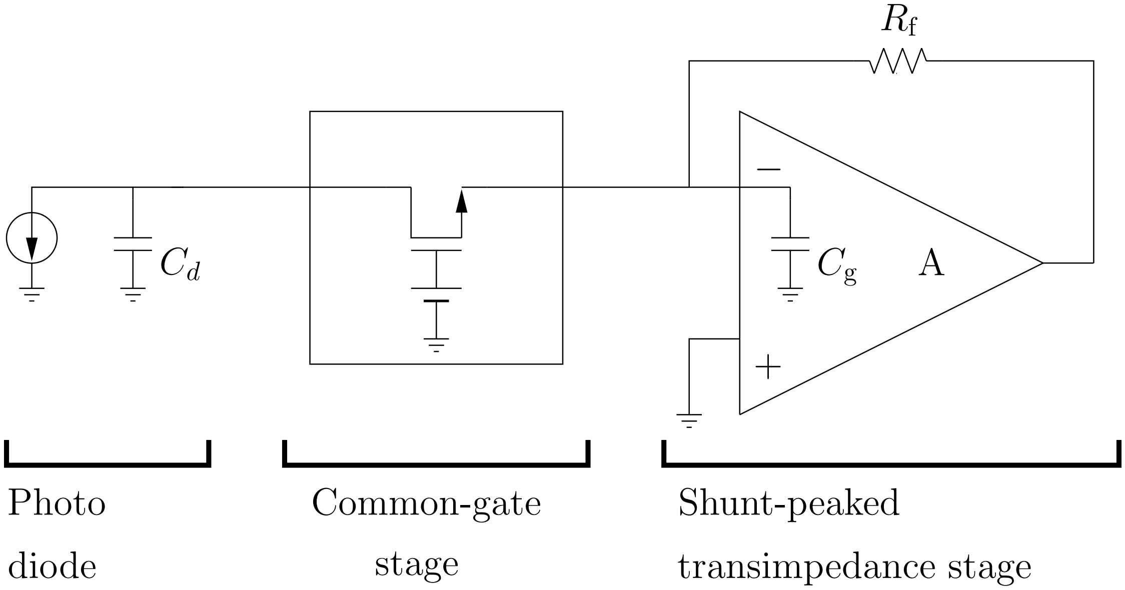

Fig. 9. Preamplifier with shunt peaking

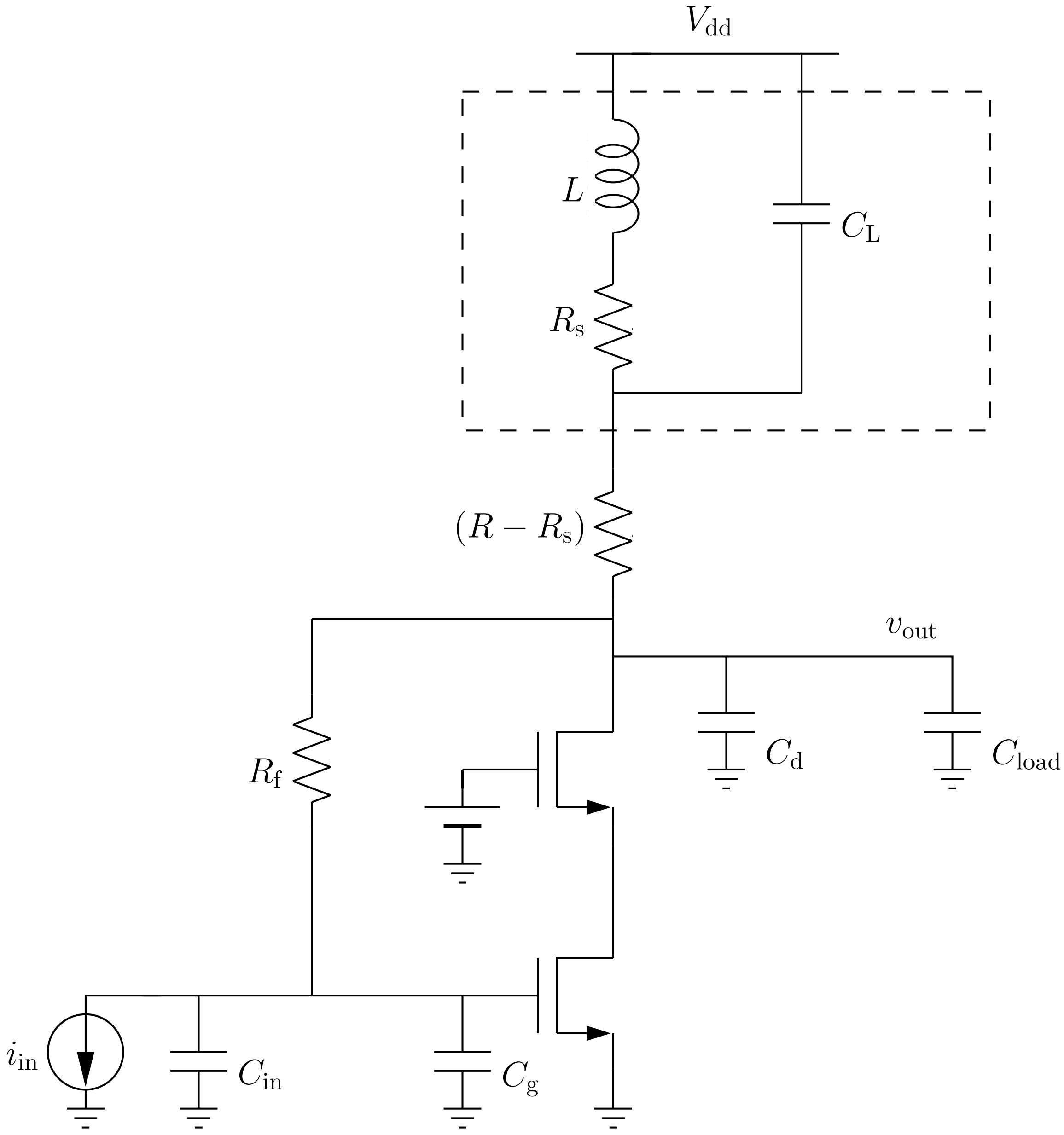

Fig. 10. Shunt-peaked transimpedance stage

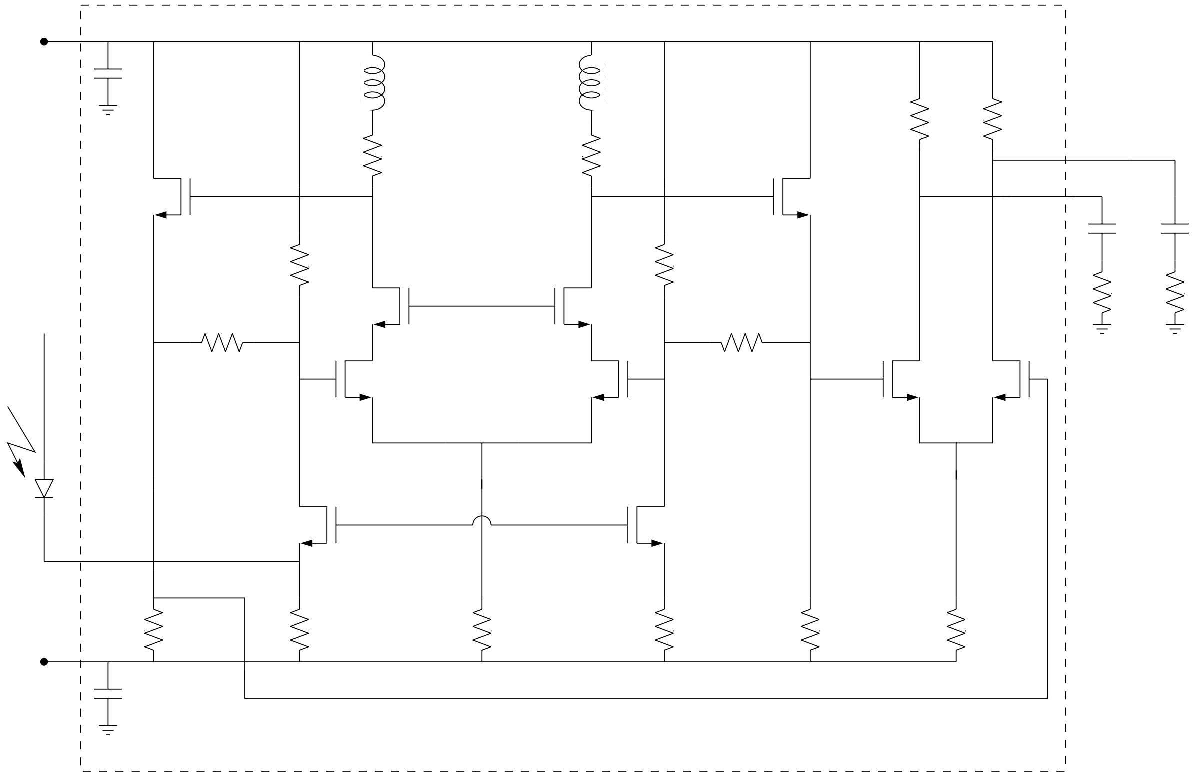

Fig. 11. Simplified Circuit Diagram

Fig. 12. Preamplifier die photo

Fig. 13. Inductor test structure

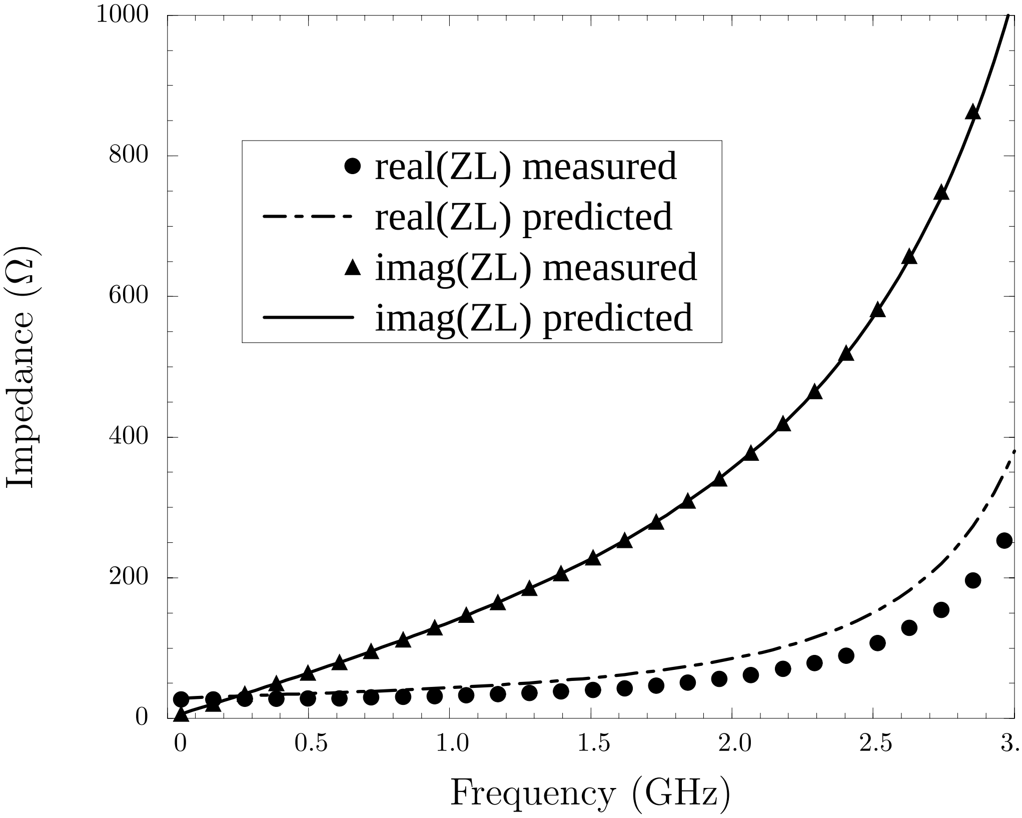

Fig. 14. Simulated and measured one-port impedance of the spiral inductor used for shunt-peaking: $d_{\text{out}} = 180\mu\text{m}$, $n = 11.75$ turns, $w = 3.2\mu\text{m}$, $s = 2.1\mu\text{m}$ and $t = 2.1\mu\text{m}$ with L

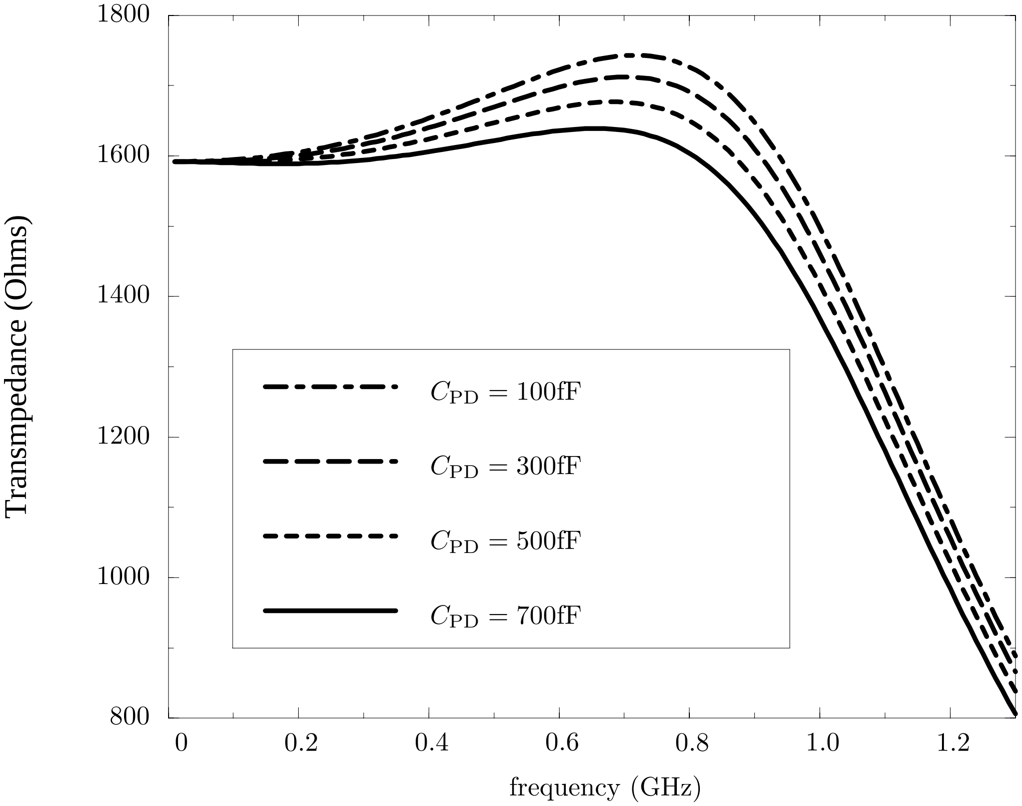

Fig. 15. Simulated transimpedance vs. frequency

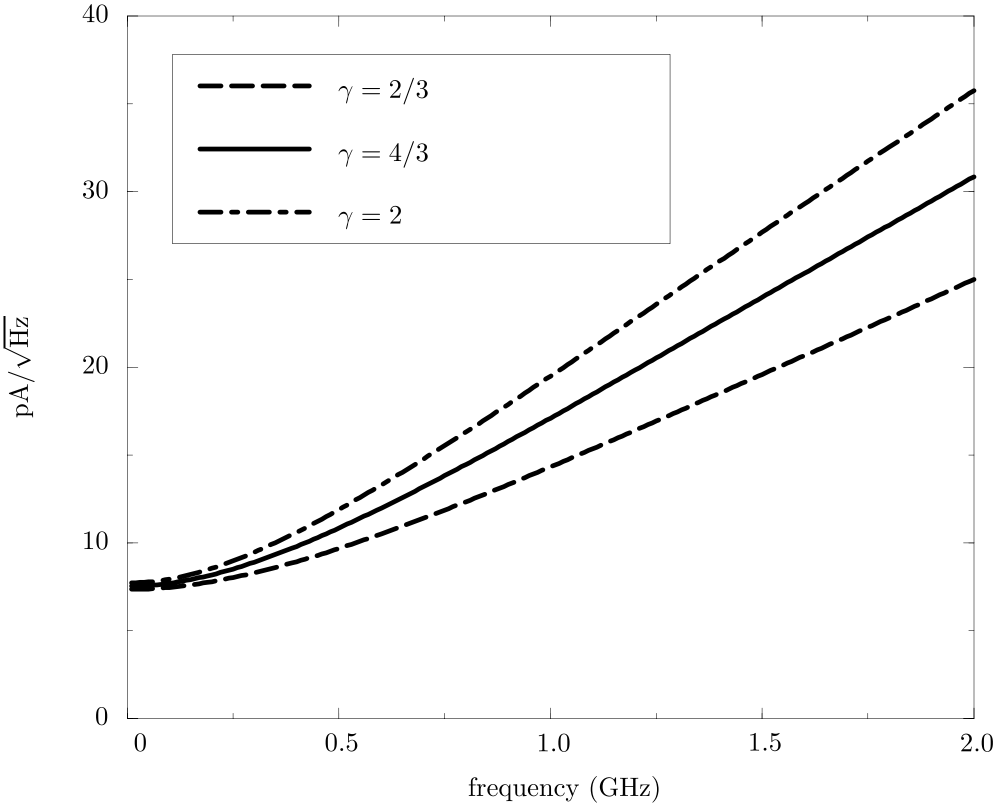

Fig. 16. Input referred current noise density

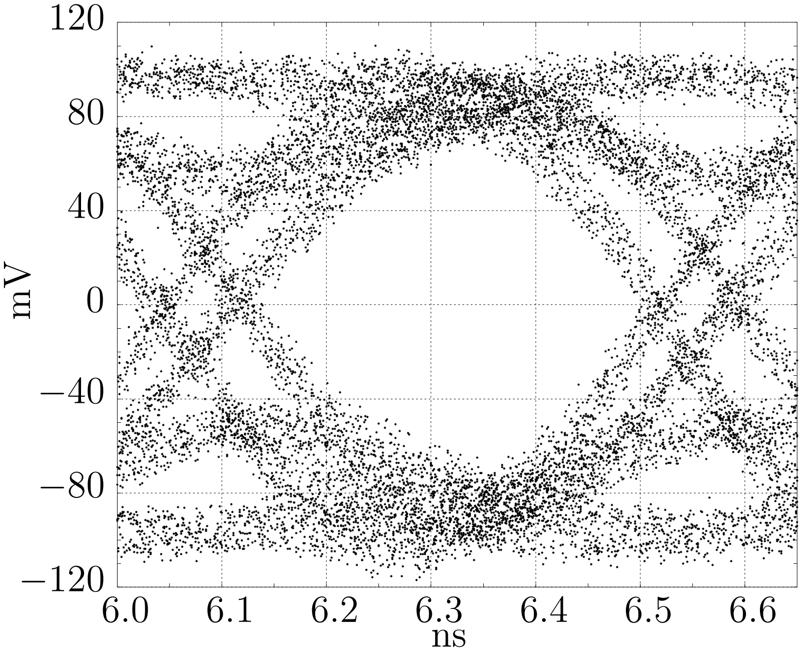

(a)

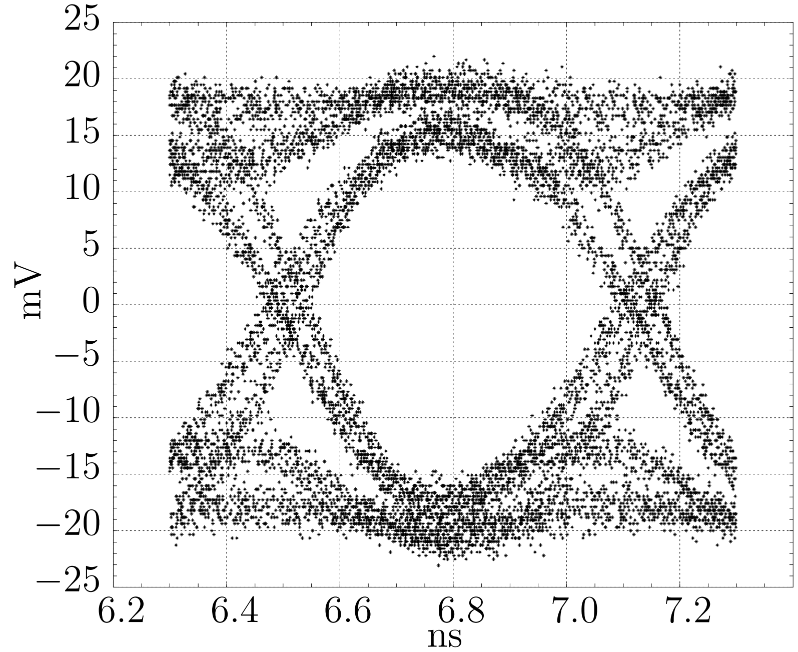

(b)

Fig. 17. Measured output eye diagrams at (a)2.1Gbaud, and at (b) 1.6Gbaud.

Factor (m)	**Normalized** ω_{3dB}	**Response**
0	1.00	No shunt peaking
0.32	1.60	Optimum group delay
0.41	1.72	Maximally flat
0.71	1.85	Maximum bandwidth

TABLE I
Benchmarks for shunt peaking

Attribute	**Bond wire**	**Planar Spiral**
Inductance	$0.5 - 4\text{nH}$	$0.2 - 100\text{nH}$
Q	$30 - 60$	< 10
Parasitics	C_{Bondpad}	R_{s}, C_{ox}, C_{si}, R_{si}
Fluctuations	Large	Small

TABLE II
Comparison of on-chip inductor realizations

Layout	c_1	c_2	c_3	c_4
Square	1.27	2.07	0.18	0.13
Hexagonal	1.09	2.23	0.00	0.17
Octagonal	1.07	2.29	0.00	0.19
Circle	1.00	2.46	0.00	0.20

TABLE III
Coefficients for current sheet expression.

Transimpedance (small-signal)	1600Ω (differential) 800Ω (single-ended)
Bandwidth (3dB)	1.2GHz
Max. photodiode capacitance	0.6pF
Max. input current	1.0mA
Simulated input noise current	0.6μA
Max. output voltage swing (50Ω load at each output)	1.0V_{pp} (differential) 0.5V_{pp} (single-ended)
Power consumption	115mW (core) 110mW (50Ω driver)
Die area	0.6mm^2
Technology	0.5μm CMOS

TABLE IV
Performance summary